

Article

Two-Dimensional Wavenumber Analysis Implemented in Ultrasonic Vector Doppler Method with Focused Transmit Beams

Hideyuki Hasegawa ^{1,*}, Masaaki Omura ¹ , Ryo Nagaoka ¹ and Kozue Saito ²¹ Faculty of Engineering, University of Toyama, Toyama 930-8555, Japan² Department of Neurology, Stroke Center, Nara Medical University, Nara 634-8522, Japan

* Correspondence: hasegawa@eng.u-toyama.ac.jp

Abstract: The multi-angle Doppler method was introduced for the estimation of velocity vectors by measuring axial velocities from multiple directions. We have recently reported that the autocorrelation-based velocity vector estimation could be ameliorated significantly by estimating the wavenumbers in two dimensions. Since two-dimensional wavenumber estimation requires a snapshot of an ultrasonic field, the method was first implemented in plane wave imaging. Although plane wave imaging is predominantly useful for examining blood flows at an extremely high temporal resolution, it was reported that the contrast in a B-mode image obtained with a few plane wave emissions was lower than that obtained with focused beams. In this study, the two-dimensional wavenumber analysis was first implemented in a framework with focused transmit beams. The simulations showed that the proposed method achieved an accuracy in velocity estimation comparable to that of the method with plane wave imaging. Furthermore, the performances of the methods implemented in focused beam and plane wave imaging were compared by measuring human common carotid arteries in vivo. Image contrasts were analyzed in normal and clutter-filtered B-mode images. The method with focused beam imaging achieved a better contrast in normal B-mode imaging, and similar velocity magnitudes and angles were obtained by both the methods with focused beam and plane wave imaging. In contrast, the method with plane wave imaging gave a better contrast in a clutter-filtered B-mode image and smaller variances in velocity magnitudes than those with focused beams.

Keywords: blood flow measurement; autocorrelation technique; vector Doppler; beam steering angle; center frequency



Citation: Hasegawa, H.; Omura, M.; Nagaoka, R.; Saito, K. Two-Dimensional Wavenumber Analysis Implemented in Ultrasonic Vector Doppler Method with Focused Transmit Beams. *Sensors* **2022**, *22*, 9787. <https://doi.org/10.3390/s22249787>

Academic Editor: Yifan Chen

Received: 17 November 2022

Accepted: 9 December 2022

Published: 13 December 2022

Publisher's Note: MDPI stays neutral with regard to jurisdictional claims in published maps and institutional affiliations.



Copyright: © 2022 by the authors. Licensee MDPI, Basel, Switzerland. This article is an open access article distributed under the terms and conditions of the Creative Commons Attribution (CC BY) license (<https://creativecommons.org/licenses/by/4.0/>).

1. Introduction

Blood flow measurement is an important practice in clinical diagnoses using ultrasonography. Color flow imaging based on the autocorrelation method [1] is a fundamental element of the function embedded in every clinical scanner and is used to map the Doppler velocities, which are the flow velocity components along the direction of ultrasonic propagation. Although a method was developed for estimation of flow-velocity vectors using Doppler velocities obtained by color flow imaging [2], the method requires assumptions based on the theory of fluid dynamics. Therefore, methods for the direct estimation of flow velocity vectors have been investigated for decades. The speckle tracking method is one of the angle-independent motion estimators and is used to estimate flow velocities [3,4]. The speckle tracking method is particularly useful in cardiac flow imaging where an ultrasonic probe with a small physical aperture must be used [5–8].

In blood flow imaging of human common carotid arteries, the physical aperture size relative to the imaging depth is significantly larger than that in cardiac imaging. In such cases, the velocity vectors can be estimated by measuring the Doppler velocities from

different directions [9–15]. These methods insonify ultrasonic beams from different directions for measurement of the Doppler velocities. Another strategy for estimation of lateral velocities was developed by Jensen and Munk, where the beamformed ultrasonic signal was modulated in the transverse direction by overlapping two receiving (Rx) beams [16]. The phase of the modulated field provides the transverse velocity of the target.

A high temporal resolution is preferable in blood flow imaging because a blood flow is a highly dynamic phenomenon. An extremely high frame rate of above a thousand frames per second is achieved by plane wave (PW) imaging [17], and the effectiveness of PW imaging in blood flow measurements was demonstrated [18,19]. The coherent plane wave compound (CPWC) was introduced to control the balance between the frame rate and image quality [20], and color flow imaging was realized at a high frame rate with the CPWC technique [21]. The angle-independent motion estimators were also combined with the CPWC technique. In the CPWC sequence, beamformed ultrasonic signals obtained from multiple PW emissions to different directions are coherently compounded. Therefore, velocity vectors can be estimated from the Doppler velocities obtained at different PW steering angles. In such methods, the velocity components along the direction of ultrasonic propagation are estimated by the spectral Doppler [22–24], autocorrelation [25–27], and speckle tracking [28–30]. Other angle-independent motion estimators, such as the transverse oscillation approach [31–33] and the frequency domain approach [34,35], were also implemented in imaging schemes with unfocused transmit (Tx) beams, which realized high frame rates.

As described above, high-frame-rate imaging is a promising method for the evaluation of blood flows. On the other hand, it is reported that contrast in a B-mode image obtained with a few plane wave emissions is lower than that obtained with focused Tx beams [20]. Another strategy to realize a high frame rate is a method called multi-line acquisition, where focused Tx beams were transmitted in multiple directions or positions simultaneously [36–38]. The multi-line acquisition was applied to myocardial motion imaging [39,40]. Recently, we have implemented the vector Doppler method in the multi-line acquisition scheme for the angle independent estimation of flow velocity in a common carotid artery [41]. However, the variance of the estimated velocities was large due to the lack of beam steering in emission.

In [41], the autocorrelation method was used to estimate the Doppler velocities. The Tx center frequency is commonly used in the autocorrelation method [27], while the Rx center frequency is required. It was shown that the errors in the axial velocity estimates were reduced using the center frequency obtained from the received signal [42–46] and the accuracy of the PW-based vector Doppler method was ameliorated using the estimated center frequency [47]. In addition, the benefit of the center frequency estimation was confirmed in the vector Doppler method with focused beam (FB) imaging [41]. Furthermore, it was recently reported that the velocity estimates obtained with the vector Doppler technique based on autocorrelation were improved further using both the center frequency and tilt angle of the wavefront obtained by estimating the wavenumbers of the beamformed ultrasonic signal in two dimensions [48]. Since the estimation of the wavenumbers requires a snapshot of the ultrasonic field, the method was first developed for PW imaging. In this study, the method presented in [48] was first implemented in the multi-line acquisition scheme with focused Tx beams. In [41], two parallel dynamically focused beams were created in reception to increase the frame rate. In this study, it was shown that such parallel receive beamforming was also required to estimate the two-dimensional wavenumbers. It was also shown theoretically that the total transmit-receive steering angle was halved from the steering angle in reception when the transmit beam was not steered. A small steering angle leads to large errors in estimated velocities [41]. This study demonstrated that the velocity estimation errors under such a small total steering angle could also be suppressed significantly by estimating the two-dimensional wavenumbers for the first time. The fundamental performance of the proposed method with the FB framework was validated by simulations with Field II [49,50]. Then, the performances of the methods implemented

in the FB and PW imaging were compared by measuring human common carotid arteries in vivo, and the benefits and shortcomings of both the strategies were discussed.

2. Materials and Methods

2.1. Tx-Rx Sequence and Beamforming

As illustrated in Figure 1, two non-steered focused Tx beams were created simultaneously to increase the frame rate. The size of the Tx aperture for each beam was empirically determined as 36 elements (element pitch: 0.2 mm), and Tukey apodization was used at a coefficient of 0.4. The two parallel Tx beams were laterally apart from each other by 60 times the element pitch. In each Tx-Rx event, echo signals were acquired with all the elements in the linear array. As described in the subsequent section, it is necessary to create multiple Rx beams in parallel to estimate the wavenumbers in two dimensions. Therefore, two parallel Rx lines were created around each Tx beam. The lateral interval of the two parallel Rx lines corresponded to the element pitch. The set of the aperture positions for the two parallel Tx beams was laterally translated by two elements after each Tx-Rx event so that the lateral intervals δx of Rx lines always corresponded to the element pitch. By acquiring echo signals at 30 different sets of the aperture positions, $(30 \text{ sets}) \times (2 \text{ Tx beams}) \times (2 \text{ Rx lines}) = 120 \text{ Rx lines}$ were created. The vertical intervals δz of the sampled beamformed signals in the Rx beamforming were set at 0.025 mm empirically.

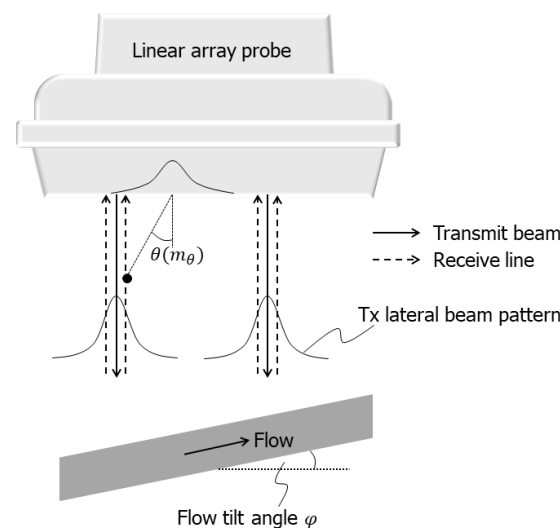


Figure 1. Illustration of measurement geometry and definitions of flow tilt angle and beam steering angle.

The complex analytic signals obtained from the echoes received with the individual elements were used for the Rx delay-and-sum (DAS) beamforming, and the dynamic focusing was performed. Quadrature detection was performed before beamforming to obtain the complex analytic signals because it was necessary to change the beamforming grid depending on the Rx beam steering angle so that the sampled data exist along the axial direction when quadrature detection was performed after Rx beamforming. To avoid such a complexity, the echo signals were converted into the analytic signals before Rx beamforming in this study.

At every sampled point in each Rx line, three Rx beams were created at different steering angles $\theta(m_\theta)$ ($m_\theta = 1, 2, \dots, M_\theta$; $M_\theta = 3$). Maximum Rx beam steering angle θ_{\max} was assigned at 10, 15, and 20 degrees, which corresponded to steering angle sets of $(-10, 0, 10)$, $(-15, 0, 15)$, and $(-20, 0, 20)$ degrees, respectively. To create the Rx beams at the respective steering angles, the peak position of the Rx apodization function (Gaussian function) was set so that the angle from the vertical direction to the direction of the vector from the peak position of the Rx apodization function to the point of interest became the corresponding steering angle as illustrated in Figure 1. The F-number was set at 2.34 in

the Rx beamforming, where the full width at half maximum of the Gaussian apodization function was defined as the aperture size.

In this study, the multi-line acquisition was performed with the repeated transmit sequence [51]. Figure 2 shows the Tx sequence used in this study. As illustrated in Figure 2, the aliasing limit, i.e., the maximum measurable velocity, remains as large as possible by correlating complex beamformed signals obtained by consecutive emissions.

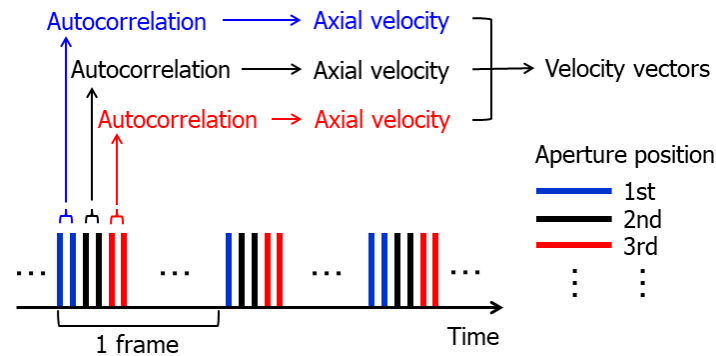


Figure 2. Illustration of transmit sequence. Tx-Rx event was repeated twice at the same aperture position, and autocorrelation was calculated using beamformed signals obtained from two consecutive emissions.

2.2. Principles for Velocity Estimation

In this study, the velocity vector estimator described in [48] was implemented in the multi-line acquisition sequence. The complex beamformed RF signal in each frame, which consists of M_x and M_z sampled points in lateral and vertical directions, respectively, is defined as $s(m_x, m_z, m_\theta, m_e)$ ($m_x = 1, 2, \dots, M_x$; $m_z = 1, 2, \dots, M_z$; $m_\theta = 1, 2, \dots, M_\theta$; $m_e = 1$ or 2). The pulse repetition number at each aperture position is denoted as m_e .

The autocorrelation function $\gamma(m_x, m_z, m_\theta)$ at a temporal lag is obtained from the complex beamformed signals as follows:

$$\gamma(m_x, m_z, m_\theta) = E_R[s^*(m_x, m_z, m_\theta, 1) \cdot s(m_x, m_z, m_\theta, 2)], \quad (1)$$

where $*$ denotes complex conjugate, and averaging operation is denoted by $E_R[\cdot]$. In this study, the lateral and vertical sizes of a kernel, which was denoted as R in Equation (1), were set at 1.0 and 0.825 mm, respectively. The Doppler velocity $v_d(m_x, m_z, m_\theta)$ is estimated as

$$\hat{v}_d(m_x, m_z, m_\theta) = \frac{c_0}{4\pi f_0 T_{\text{PRI}}} \angle \gamma(m_x, m_z, m_\theta), \quad (2)$$

where c_0 , f_0 , \angle , and T_{PRI} denote the speed of sound, ultrasonic center frequency, phase angle of a complex value, and pulse repetition interval (PRI), respectively.

As described in Equation (2), the center frequency f_0 of the received signal is required to estimate the Doppler velocity. In this study, the method presented in [48] was used to obtain the center frequency f_0 by estimating the wavenumbers of the beamformed signal in two dimensions.

The axial wavenumber k and center frequency f_0 are estimated as

$$\hat{f}_0 = \frac{c_0}{2\pi} \hat{k} = \frac{c_0}{2\pi} \sqrt{\hat{k}_x^2 + \hat{k}_z^2}, \quad (3)$$

where k_x and k_z are the lateral and vertical wavenumbers, respectively, and $\hat{\cdot}$ denotes an estimate. The tilt angle $\phi(m_x, m_z, m_\theta)$ of the wavefront in the beamformed signal is also estimated as

$$\hat{\phi}(m_x, m_z, m_\theta) = \tan^{-1} \frac{\hat{k}_x}{\hat{k}_z}. \quad (4)$$

To estimate the vertical wavenumber k_z , the autocorrelation function $\gamma_z(m_x, m_z, m_\theta)$ at a vertical lag is expressed as

$$\gamma_z(m_x, m_z, m_\theta) = E_R[s^*(m_x, m_z, m_\theta, 1) \cdot s(m_x, m_z + 1, m_\theta, 1)]. \tag{5}$$

The vertical wavenumber k_z can be estimated from the change in the phase of the beamformed signal during sampling interval δz in the vertical direction, which corresponds to the phase of the autocorrelation function $\gamma_z(m_x, m_z, m_\theta)$ at a vertical lag. Thus, the vertical wavenumber k_z is estimated as

$$\hat{k}_z = \frac{\angle \gamma_z(m_x, m_z, m_\theta)}{2\delta z}. \tag{6}$$

Similarly, the lateral wavenumber k_x is estimated by evaluating the autocorrelation function $\gamma_x(m_x, m_z, m_\theta)$ at a lateral lag defined as

$$\gamma_x(m_x, m_z, m_\theta) = E_R[s^*(m'_x, m_z, m_\theta, 1) \cdot s(m'_x + 1, m_z, m_\theta, 1)], \tag{7}$$

$$m'_x = \left\lfloor \frac{m_x - 1}{2} \right\rfloor + 1, \tag{8}$$

where $\lfloor \cdot \rfloor$ denotes omission of fractions. In the estimation of the lateral wavenumber k_x , it is important to evaluate the autocorrelation function of the beamformed signals obtained from the same Tx beam because the phase of the autocorrelation function $\gamma_x(m_x, m_z, m_\theta)$ includes the phase alterations induced by both the tilt of the wavefront and the target motion when it is evaluated from the beamformed signals obtained from different Tx beams. Therefore, the lateral sampling number m'_x in Equation (7) was determined by Equation (8) so that the autocorrelation function $\gamma_x(m_x, m_z, m_\theta)$ was calculated using the beamformed signals obtained from the same Tx beam (two parallel Rx beams were created in the RX beamforming). The lateral wavenumber k_x is estimated as

$$\hat{k}_x = \frac{\angle \gamma_x(m_x, m_z, m_\theta)}{2\delta x}. \tag{9}$$

As described in [9,27], the lateral and vertical velocities $v_x(m_x, m_z)$ and $v_z(m_x, m_z)$ in each frame are described as

$$v_x(m_x, m_z) \{ \sin \theta_t(m_\theta) + \sin \theta_r(m_\theta) \} + v_z(m_x, m_z) \{ \cos \theta_t(m_\theta) + \cos \theta_r(m_\theta) \} = 2v_d(m, m_z, m_\theta), \tag{10}$$

where $\theta_t(m_\theta)$ and $\theta_r(m_\theta)$ are the Tx and Rx beam steering angles, respectively. A matrix form of the relationships obtained at M_θ different steering angles is expressed as

$$\begin{aligned} & \begin{bmatrix} \sin \theta_t(1) + \sin \theta_r(1) & \cos \theta_t(1) + \cos \theta_r(1) \\ \vdots & \vdots \\ \sin \theta_t(M_\theta) + \sin \theta_r(M_\theta) & \cos \theta_t(M_\theta) + \cos \theta_r(M_\theta) \end{bmatrix} \\ & \times \begin{bmatrix} v_x(m_x, m_z) \\ v_z(m_x, m_z) \end{bmatrix} = \begin{bmatrix} 2\hat{v}_d(m_x, m_z, 1) \\ \vdots \\ 2\hat{v}_d(m_x, m_z, M_\theta) \end{bmatrix} \\ & \Rightarrow \mathbf{A}\mathbf{v} = \hat{\mathbf{v}}_{ax}. \end{aligned} \tag{11}$$

The solution of Equation (11) is obtained by the least-square method as

$$\hat{\mathbf{v}} = \left(\mathbf{A}^T \mathbf{A} \right)^{-1} \mathbf{A}^T \hat{\mathbf{v}}_{ax}, \tag{12}$$

where $\left(\mathbf{A}^T \mathbf{A} \right)^{-1} \mathbf{A}^T$ corresponds to the pseudoinverse of \mathbf{A} .

2.3. Consideration on Beam Steering Angle in Estimation of Axial Velocity

As described in Equation (11), the Tx and Rx beam steering angles $\theta_t(m_\theta)$ and $\theta_r(m_\theta)$ are required to estimate the velocity vector. In the vector Doppler method, the predefined steering angles are commonly used [27,41,47]. This means that $\theta_t(m_\theta) = 0$ and $\theta_r(m_\theta) = \theta(m_\theta)$ in the proposed FB framework. However, the tilt angle of the wavefront in the beamformed signal should be considered because the phase shift of the beamformed signal depends on the tilt angle of the wavefront, as illustrated in Figure 3. The tilt angle of the wavefront in the beamformed signal simply corresponds to the beam steering angle when the Tx and Rx steering angles are the same, as is investigated in [48]. On the other hand, the Tx and Rx steering angles are different in this study. Let us consider the tilt angle of the wavefront in such a situation.

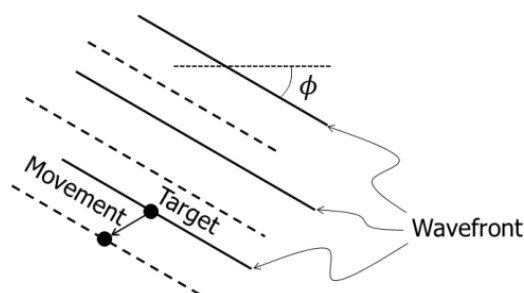


Figure 3. Illustration of target movement in beamformed signal with tilted wavefront. The solid and dashed lines show pre- and post-motion wavefronts, respectively.

By assuming that the wavefront is locally planar, the ultrasonic field $g(x, z)$ produced from a point target in a Tx or Rx event is simply modelled as

$$g(x, z) = \exp\left(-\frac{x^2}{\sigma_{tr}^2} - \frac{z^2}{\sigma_{ax}^2}\right) \cdot \exp\{j(k_x x + k_z z)\}, \tag{13}$$

where σ_{tr}^2 and σ_{ax}^2 determine the spread of the Gaussian envelope of the field in the direction of the wavefront and the direction transverse to the wavefront, which depend on the beam width and pulse length, respectively. Although the Gaussian envelope should also be tilted in the case of a steered beam, the tilt of the envelope was omitted because the direction of the wavefront was important in this study.

Since the Tx and Rx beam steering angles are 0 and $\theta(m_\theta)$, respectively, the ultrasonic fields $g_t(x, z)$ and $g_r(x, z)$ in Tx and Rx are respectively expressed as

$$g_t(x, z) = \exp\left(-\frac{x^2}{\sigma_{tr}^2} - \frac{z^2}{\sigma_{ax}^2}\right) \cdot \exp(jkz), \tag{14}$$

$$g_r(x, z) = \exp\left(-\frac{x^2}{\sigma_{tr}^2} - \frac{z^2}{\sigma_{ax}^2}\right) \times \exp[jk\{x \sin \theta(m_\theta) + z \cos \theta(m_\theta)\}]. \tag{15}$$

With the far field approximation, the Tx-Rx field $g_{t-r}(x, z)$ is expressed by the product of $g_t(x, z)$ and $g_r(x, z)$ as [52]

$$g_{t-r}(x, z) = \exp\left(-\frac{2x^2}{\sigma_{tr}^2} - \frac{2z^2}{\sigma_{ax}^2}\right) \times \exp[jk\{x \sin \theta(m_\theta) + z(1 + \cos \theta(m_\theta))\}]. \tag{16}$$

Therefore, the tilt angle ϕ of the wavefront in the beamformed signal (pulse-echo field) is obtained as

$$\phi = \tan^{-1} \left\{ \frac{\sin \theta(m_\theta)}{1 + \cos \theta(m_\theta)} \right\} = \frac{\theta(m_\theta)}{2}. \tag{17}$$

As can be seen in Equation (17), the tilt angle of the wavefront is different from the predetermined beam steering angle (zero or $\theta(m_\theta)$). As illustrated in Figure 3, the target

motion induces the phase shift along the direction transverse to the wavefront in the Tx-Rx field and thus the direction of the estimated Doppler velocity corresponds to this direction. Therefore, in the estimation of velocity vectors in Equation (12), the beam steering angles were set at $\theta_t(m_\theta) = \theta_r(m_\theta) = \hat{\phi}(m_x, m_z, m_\theta)$, where the tilt angle $\hat{\phi}(m_x, m_z, m_\theta)$ of the wavefront was directly estimated from the beamformed signal using Equation (4).

2.4. Clutter Filtering

Clutter filtering based on singular value decomposition (SVD) was performed on the beamformed signals to suppress strong echoes from surrounding tissues and enhance weak echoes from blood cells [41,53]. In the clutter filtering, the beamformed signals obtained with the same steering angle and emission number were grouped for the SVD processing to create datasets with a regular frame interval. In other words, the beamformed signals obtained with different steering angles and emission numbers were processed by SVD separately. In each SVD processing, all 180 frames (approximately 1 s) were processed at once. By inspecting the singular value profiles, the threshold values were assigned empirically to indicate echoes from tissues and blood cells and electrical noise.

2.5. Numerical Simulations

The accuracy of the proposed velocity estimator was validated by Field II simulations [49,50]. A 192-element linear array probe was simulated. The element pitch was set at 0.2 mm. Each element emits an ultrasonic pulse of a 3-cycle sinusoidal wave at 4.8 MHz. A Hanning function was used for its envelope. The transmit sequence described in Section 2.1 was implemented, and the echoes from the simulated phantom were received by all the 192 elements. The received signals were stored at a sampling frequency of 31.25 MHz. The pulse repetition frequency (PRF) was set at 10 kHz.

The numerical phantom was generated by distributing point scatterers randomly in a cylindrical shape of 5 mm in diameter. Since a tilt angle of a common carotid artery is generally less than 10 degrees, the flow tilt angle φ of the cylindrical phantom was set at 0, 5, and 10 degrees. The scatterer number density was set at 30.3 scatterers/mm³ [24], and the attenuation coefficient was set at 0.5 dB/cm/MHz. The distributed scatterers were moved at a constant speed along the longitudinal direction of the cylindrical shape. Parabolic velocity profiles were assigned, where the moving velocities of the scatterers at the radial periphery of the cylindrical shape were set at zero. The moving velocity was maximum at the center of the transverse section of the phantom. Maximum velocity v_{\max} was altered from 100 to 1000 mm/s.

2.6. Experimental Setup

The feasibility of the proposed method in in vivo imaging was demonstrated by measurements of human common carotid arteries of two healthy subjects. This study was approved by the institutional ethical committee and was performed with the informed consent of the subjects.

A custom-made scanner (RSYS0016, Microsonic, Tokyo, Japan) with a 192-element linear array probe (UST-5412, Fujifilm, Tokyo, Japan) was used for in vivo measurements. The element pitch of the linear array was 0.2 mm. The echo signals from the carotid arteries were acquired with the Tx sequence described in Section 2.1. Each element was excited with a rectangular pulse at a center frequency of 4.8 MHz, and the PRI was set at 96 ms, which corresponded to a PRF of 10,417 kHz. The echo signals were received by all the 192 elements and sampled at 31.25 MHz. The settings in the simulations and in vivo measurements are summarized in Table 1.

Table 1. Parameters in simulations and in vivo measurements.

Parameters	Value
Tx center Frequency	4.8 MHz
Element pitch	0.2 mm
PRF	10 kHz (simulation) 10.417 kHz (in vivo)
Sampling frequency	31.25 MHz
Rx F-number	2.34
Correlation kernel size	x: 1.0 mm, z: 0.825 mm
Ensemble size	1–8 (simulation), 4, 8 (in vivo)

2.7. Metrics for Evaluation of Accuracy in Velocity Estimation

In the simulations, the absolute bias error (ABE) and root mean squared error (RMSE) were used for evaluation of the accuracy in velocity estimation. The ABE and RMSE are defined as

$$ABE = \frac{\left| \mathbb{E}_{R_f} \left[\hat{\mathbf{v}} - \mathbf{v}_{\text{tru}} \right] \right|}{\left| \mathbb{E}_{R_f} [\mathbf{v}_{\text{tru}}] \right|}, \quad (18)$$

$$RMSE = \frac{\sqrt{\mathbb{E}_{R_f} \left[\left| \hat{\mathbf{v}} - \mathbf{v}_{\text{tru}} \right|^2 \right]}}{\left| \mathbb{E}_{R_f} [\mathbf{v}_{\text{tru}}] \right|}, \quad (19)$$

where R_f and \mathbf{v}_{tru} denote the region with the flow phantom and true velocity vector, respectively. In the simulations, the three methods described below were examined to evaluate the effects of the center frequency and steering angle separately:

1. Method 1: w/o f_0 estimation, $\theta_t(m_\theta) = 0$, $\theta_r(m_\theta) = \theta(m_\theta)$
2. Method 2: w/ f_0 estimation by Equation (3), $\theta_t(m_\theta) = 0$, $\theta_r(m_\theta) = \theta(m_\theta)$
3. Method 3: w/ f_0 estimation by Equation (3), $\theta_t(m_\theta) = \theta_r(m_\theta) = \hat{\varphi}(m_x, m_z, m_\theta)$ from Equation (4)

In Method 1, a constant value of 4.3 MHz was assigned as the center frequency over the entire region of interest by referring to ones estimated from the simulated data using Equation (3). Since the steered beams are used in the vector Doppler method, the fully beamformed region is narrowed due to the finite size of the linear array when the steering angle is increased. Therefore, the errors were evaluated within a lateral width of ± 4.5 mm around the center of the field of view [48].

3. Results

3.1. Simulations

3.1.1. Estimation of Tilt Angle of Wavefront

As described in Section 2.3, the tilt angle of the wavefront in the beamformed signal would be different from the Tx or Rx beam steering angle when the Tx and Rx steering angles are different. Therefore, the tilt angles of the wavefronts were first examined at different maximum Rx beam steering angles θ_{max} . Figure 4a–c show the estimated tilt angles of the wavefronts in the beamformed signal under Rx steering angles of -20 , 0 , and 20 degrees, respectively. The flow tilt angle φ was set at 0 degrees.

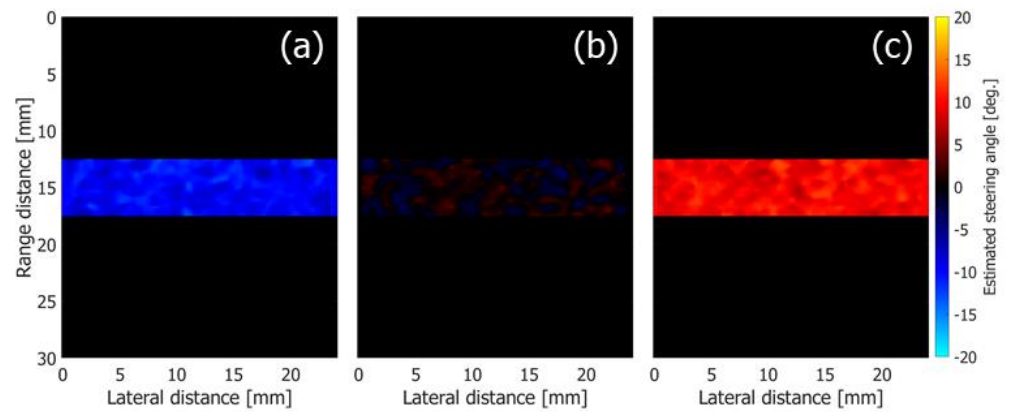


Figure 4. Estimated tilt angles of wavefronts obtained at respective Rx steering angles. (a) -20 degrees. (b) 0 degrees. (c) 20 degrees.

Although the Rx beam steering angles in Figure 4a,c are set at -20 and 20 degrees, respectively, the estimated tilt angles are different from the preassigned Rx steering angles as described in Section 2.3. The means and standard deviations of the estimated tilt angles of the wavefront in the beamformed signals were obtained at the different Rx beam steering angles and are shown by the plots and vertical bars in Figure 5, respectively. The dashed line shows the theoretical value obtained by Equation (17). Although the absolute values of the estimated tilt angles are slightly lower than the theoretical values, the estimated values are in good agreement with the theoretical ones. As described in Section 2.3, the estimated tilt angle $\hat{\phi}(m_x, m_z, m_\theta)$ of the wavefront was used in the proposed method (Method 3) for estimation of velocity vectors.

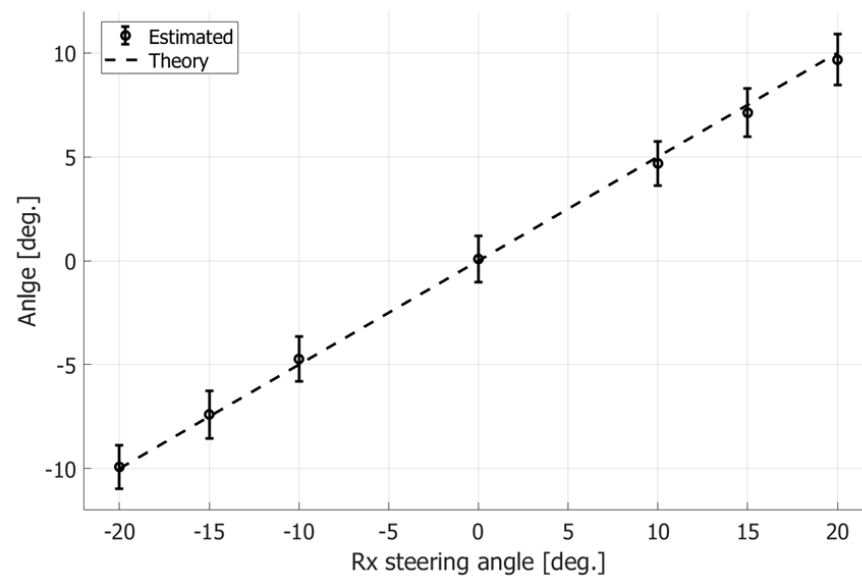


Figure 5. Estimated and theoretical tilt angles of wavefronts obtained at different Rx steering angles.

3.1.2. Accuracy in Velocity Estimation

In Figure 6, the plots and vertical bars respectively show the means and standard deviations of the velocity magnitudes, which were estimated under flow tilt angle φ and maximum velocity v_{\max} of 0 degrees and 100 mm/s, respectively. The red dashed line shows the true velocity profile. In Figure 6I–III, maximum Rx beam steering angles θ_{\max} are set at 10 , 15 , and 20 degrees, respectively, and the estimates in Figure 6(1–3) are obtained with Methods 1, 2, and 3, respectively.

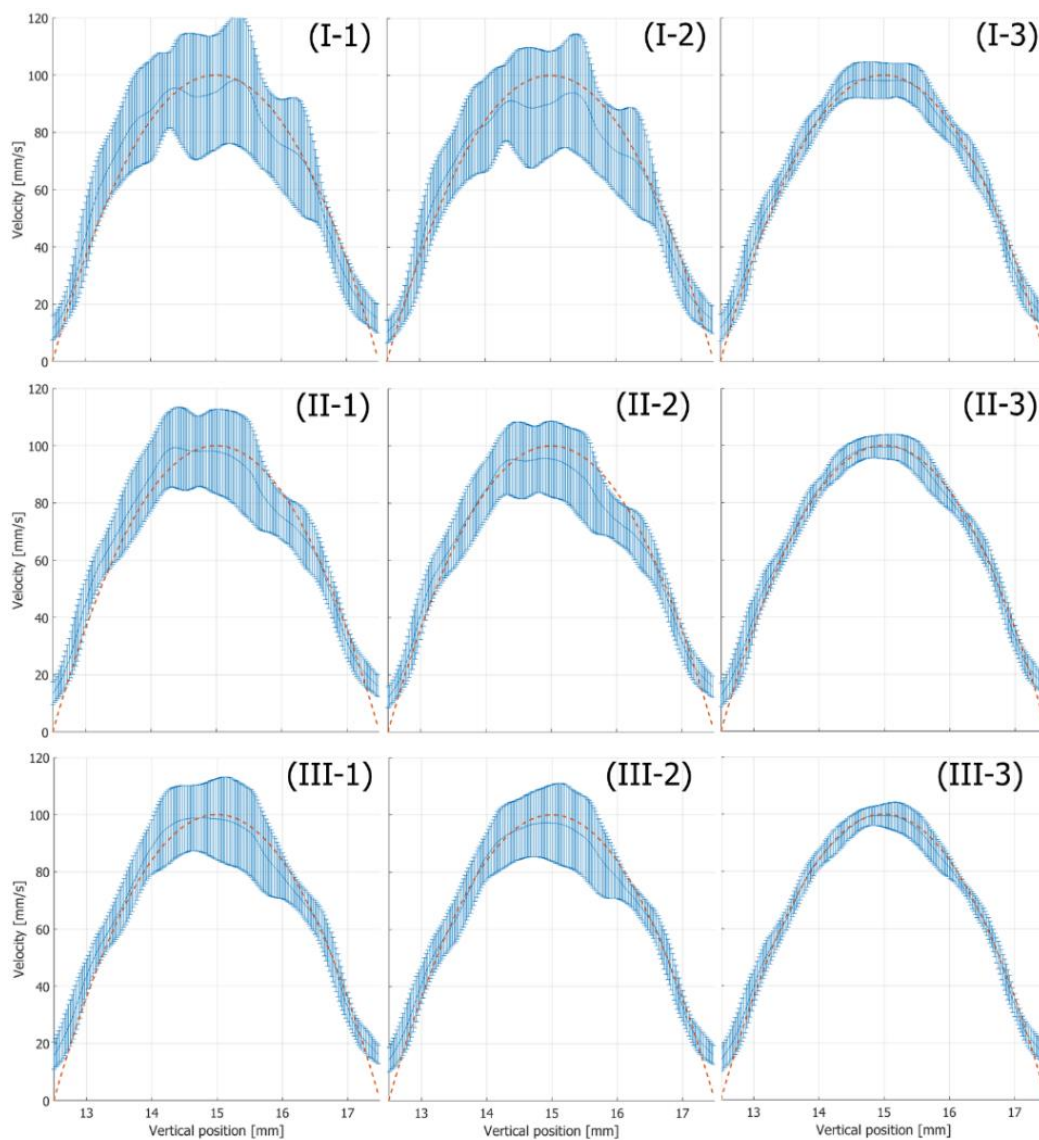


Figure 6. Means and standard deviations of estimated velocity magnitudes (flow tilt angle: 0 degrees, maximum velocity: 100 mm/s). The red dashed line shows the true velocity profile. The plots and vertical bars show means and standard deviations of estimated velocities, respectively. Results were obtained with Method 1 (I-1,II-1,III-1), Method 2 (I-2,II-2,III-2), and Method 3 (I-3,II-3,III-3). Rx beam steering angles were set at 10 (I-1–I-3), 15 (II-1–II-3), and 20 (III-1–III-3) degrees.

In comparison with the velocity estimates obtained by Method 1 in Figure 6(1), the standard deviations are slightly reduced by estimating the local center frequencies in the beamformed signal using Method 2, as can be seen in Figure 6(2). However, the standard deviations are still large. The standard deviations are reduced significantly using both the center frequency and tilt angle of the wavefront using Method 3, as can be seen in Figure 6(3). Figure 7 summarizes the ABEs and RMSEs obtained by the respective methods. The boxes and vertical bar represent the ABEs and RMSEs, respectively. As can be seen in Figure 7, Method 3 (proposed method) achieved a significantly better performance than Methods 1 and 2. In addition, the proposed method achieved the best performance with an Rx steering angle θ_{\max} of 20 degrees. Therefore, the proposed method was used with setting θ_{\max} to 20 degrees in the subsequent examinations.

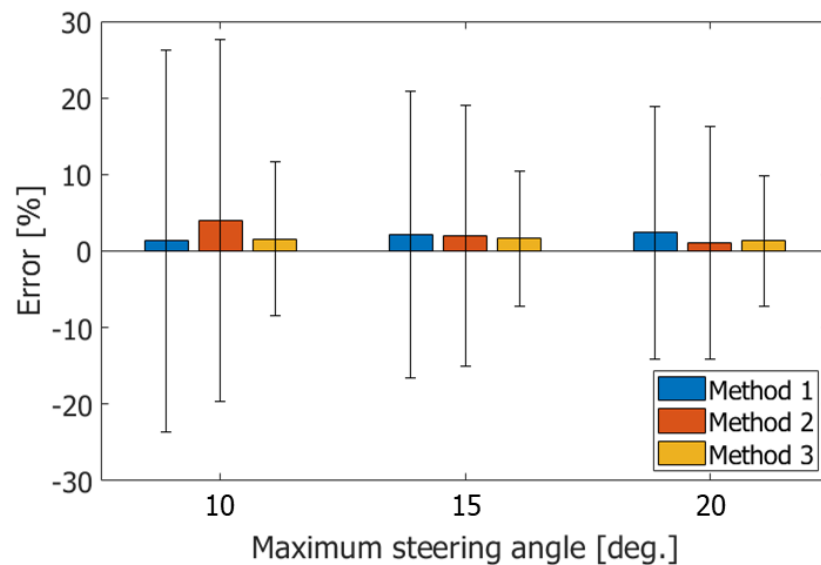


Figure 7. ABEs and RMSEs in estimated velocities obtained with respective methods.

The performance of the proposed method was also evaluated under other conditions. In Figure 8, the ABEs and RMSEs are evaluated at different flow tilt angles φ (0, 5, and 10 degrees) and maximum velocities v_{\max} (100, 250, 500, 750, and 1000 mm/s) are shown by the boxes and vertical bars, respectively. The velocities were estimated with RMSEs of around 10% under different flow tilt angles and maximum flow velocities.

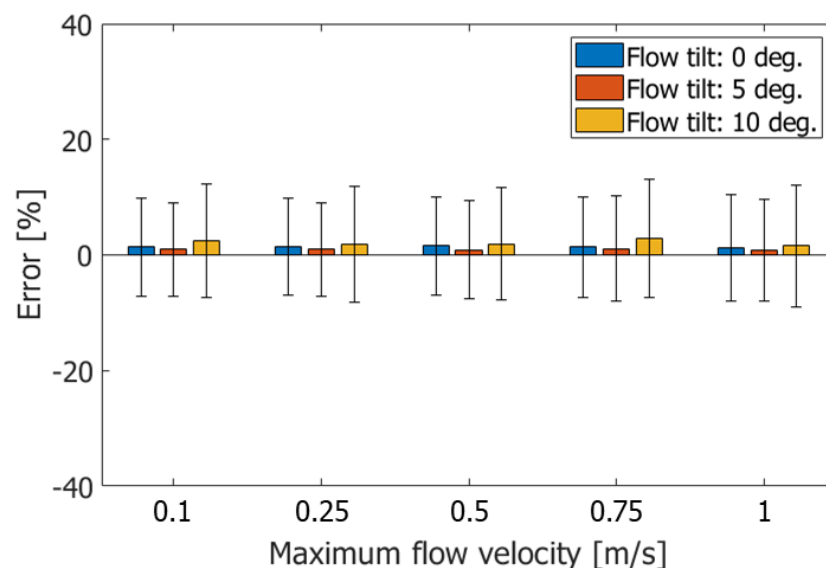


Figure 8. ABEs and RMSEs in estimated velocities obtained with Method 3 at Rx beam steering angle of 20 degrees.

Figure 9 shows the ABEs and RMSEs in the velocities obtained at different signal-to-noise ratios (SNRs). The SNR was altered by adding random noise to the simulated beamformed signal. The flow tilt angle φ and maximum velocity v_{\max} were the same as those in Figure 7. As can be seen in Figure 9, the errors increase with decreasing the SNR. In conventional color flow imaging, ensemble averaging is commonly used to reduce the variance in estimated velocities. The errors were also evaluated with the ensemble averaging of the complex correlation functions for eight frames and shown in Figure 9. As can be seen in Figure 9, the ensemble averaging is effective to reduce the variance in the estimated velocities even in the proposed method.

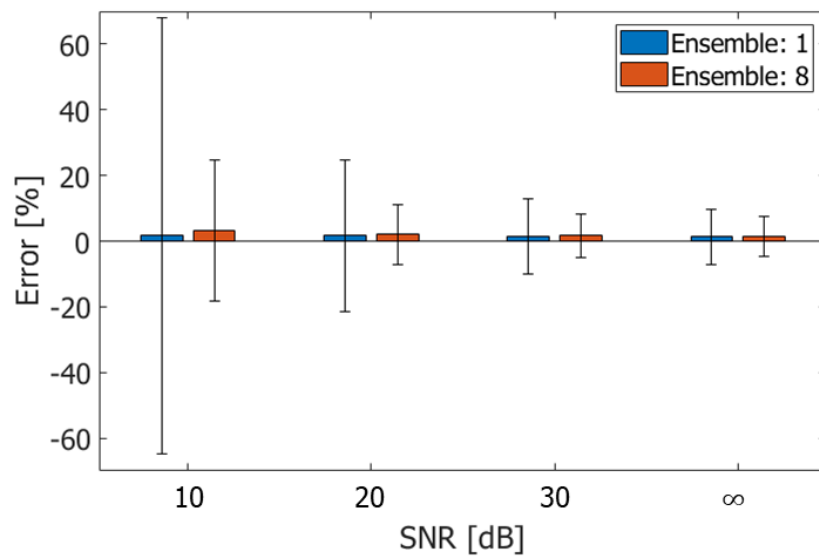


Figure 9. ABEs and RMSEs evaluated by estimating velocities without and with ensemble averaging. The errors are evaluated under different SNRs.

3.2. In Vivo Measurements

As a velocity estimator itself, it was shown by the simulations that the proposed method with focused Tx beams achieved an accuracy in velocity estimation, which was comparable to the method with PW imaging [48]. The feasibility of the proposed method in in vivo imaging and comparison of the methods implemented in FB and PW imaging were investigated by measuring human common carotid arteries in vivo.

Figure 10(1-a,2-a) show B-mode images of the common carotid arteries of 48-year-old and 26-year-old healthy male subjects, respectively. Figure 10(1-b,2-b) show B-mode images of the 48-year-old and 26-year-old subjects, respectively, obtained from the clutter-filtered beamformed signals.

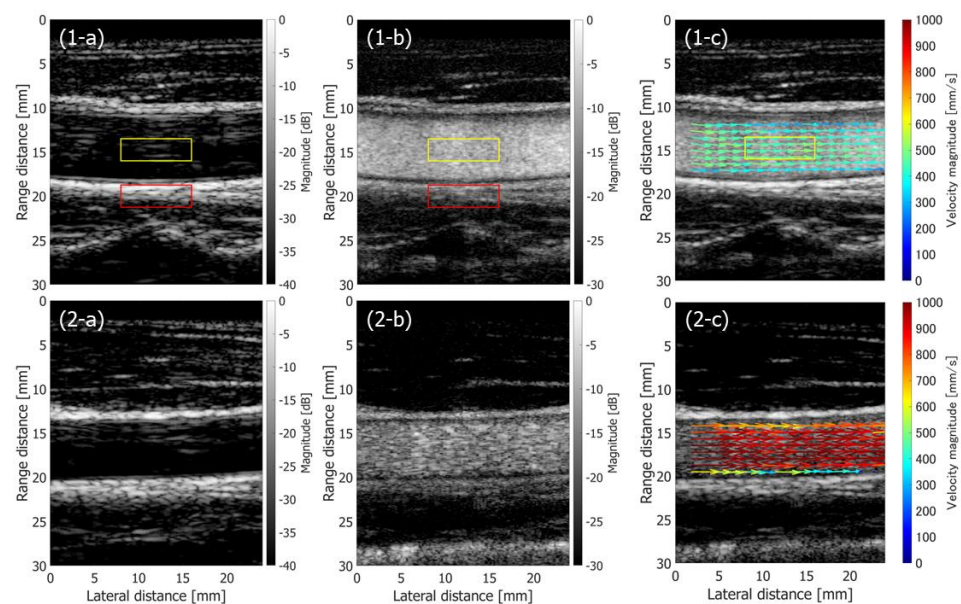


Figure 10. Results on in vivo measurements of 48-year-old (1-a,1-b,1-c) and 26-year-old (2-a,2-b,2-c) healthy subjects obtained with the Tx-Rx sequence developed in this study. (1-a,2-a) Normal B-mode images. (1-b,2-b) Clutter-filtered B-mode images. (1-c,2-c) Flow velocity vectors estimated in cardiac systolic phase are overlaid on blood speckle images. The red and yellow boxes show regions used for evaluation of contrast.

The clutter-filtered signals were analyzed with Method 3 at Rx maximum beam steering angle θ_{\max} of 20 degrees. The arrows in Figure 10(1-c,2-c) show the flow velocity vectors in the carotid arteries of the 48-year-old and 26-year-old subjects, respectively, obtained in cardiac systolic phase. The arrows are overlaid on the corresponding blood speckle images. The blood speckle images were obtained by the incoherently summed non-filtered and clutter-filtered beamformed signals. In Figure 10, the complex correlation functions are averaged for eight frames (46.08 ms) before estimating the velocities. As shown in Figure 10(1-c,2-c), systolic flow velocities of around 1000 mm/s are found in the result on the 26-year-old subject, while that of the 48-year-old subject is around 600 mm/s. Physiologically consistent systolic flow velocities and age-related difference in flow velocities are reported in the literature [54], and thus the proposed method is considered feasible in in vivo applications.

Then, the performance of the proposed method in the FB sequence was compared with the method implemented in PW imaging [48]. Figure 11a–c show a normal B-mode image, a clutter-filtered B-mode image, and velocity vectors in cardiac systolic phase overlaid on a blood speckle image obtained from the same 48-year-old subject using the method with PW imaging. The Tx-Rx sequence is described in [48]. The complex correlation functions were averaged for 46.08 ms (80 frames), which was the same as that in Figure 10. It should be noted that the frame rate in the PW imaging was ten times higher than that in the FB imaging.

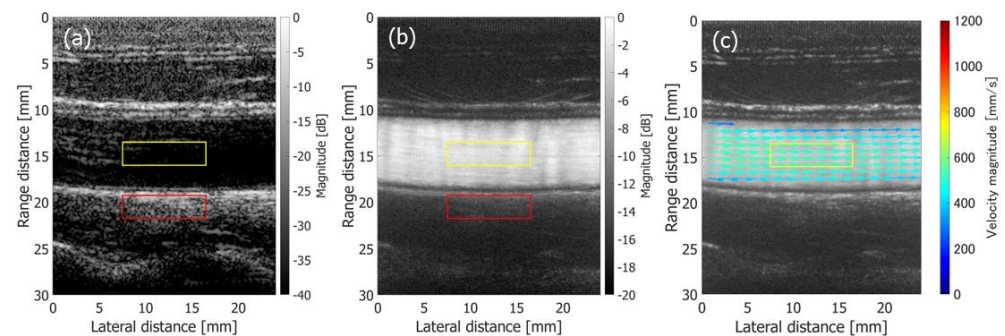


Figure 11. Results on in vivo measurement of a 48-year-old healthy subject obtained with PW imaging [48]. (a) Normal B-mode image. (b) Clutter-filtered B-mode image. (c) Flow velocity vectors estimated in cardiac systolic phase are overlaid on blood speckle image.

First the contrast between the vessel lumen and surrounding tissue in the B-mode image (both non-filtered and clutter-filtered) was evaluated. A better contrast in a non-filtered B-mode image would benefit the observation of surrounding tissues including the arterial wall. On the other hand, a better suppression of clutter signals would result in a better contrast in a clutter filtered B-mode image. The contrast between the vessel lumen and surrounding tissue was evaluated as

$$contrast = \left| 20 \log_{10} \frac{\mu_L}{\mu_T} \right| [dB], \quad (20)$$

where μ_L and μ_T are the mean echo amplitudes in the regions of interest (ROIs) assigned in the vessel lumen and surrounding tissue, as respectively indicated by the yellow and red rectangles in Figure 10(1-a,1-b) and Figure 11a,b.

Figure 12a,b show the temporal changes in the contrast values obtained from non-filtered and clutter-filtered B-mode images, respectively. Different durations (23.04 ms and 46.08 ms) for averaging the complex correlation functions were examined. The contrast of the non-filtered B-mode image obtained with FB imaging was significantly higher than that obtained with PW imaging. The contrast of the clutter-filtered B-mode image with FB imaging was slightly higher in the slow-flow phase than that with PW imaging, while the contrast with FB imaging was significantly reduced in the fast-flow phase.

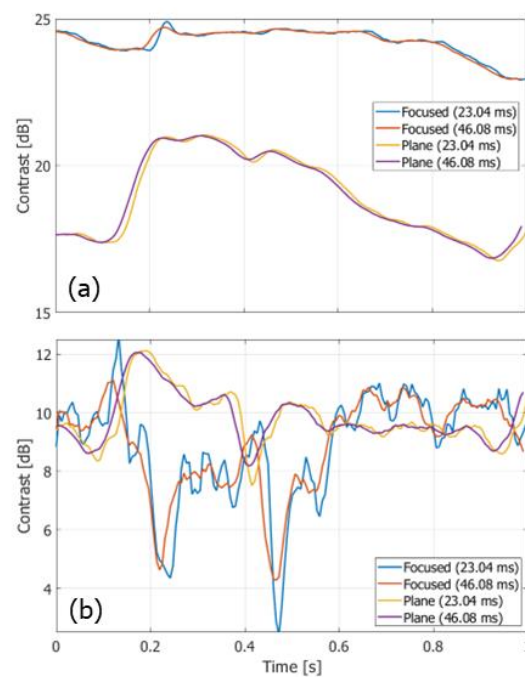


Figure 12. Temporal change in contrast values obtained from non-filtered (a) and clutter-filtered (b) B-mode images.

The variances of the velocity vectors estimated with FB and PW imaging were also compared. The ROIs were assigned as indicated in Figure 10(1-c) and Figure 11c, where the velocity distributions were relatively homogeneous. The mean and standard deviation in the magnitudes and angles of the velocity vectors were evaluated at each vertical position in the ROI from the velocity vectors estimated in different vertical lines at the corresponding vertical position. Figures 12 and 13 show the temporal changes in the means and standard deviations of the magnitudes and angles at the central vertical position in the ROI, respectively. Figures 14 and 15 show the spatial profiles of the means and standard deviations in the velocity magnitude and angles along the vertical axis, respectively, at the time when the mean velocity magnitude is maximum. In Figures 13–16, the means and standard deviations are shown by the plots and vertical bars, respectively.

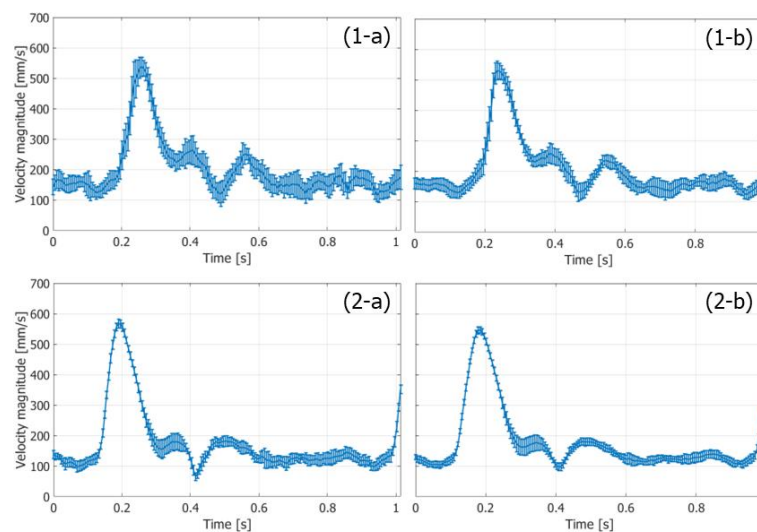


Figure 13. Temporal changes in means (plots) and standard deviations (vertical bars) of magnitudes of velocity vectors at vertical center of ROI. (1-a,1-b) FB imaging. (2-a,2-b) PW imaging [48]. (1-a,2-a) Ensemble length of 23.04 ms. (1-b,2-b) Ensemble length of 46.04 ms.

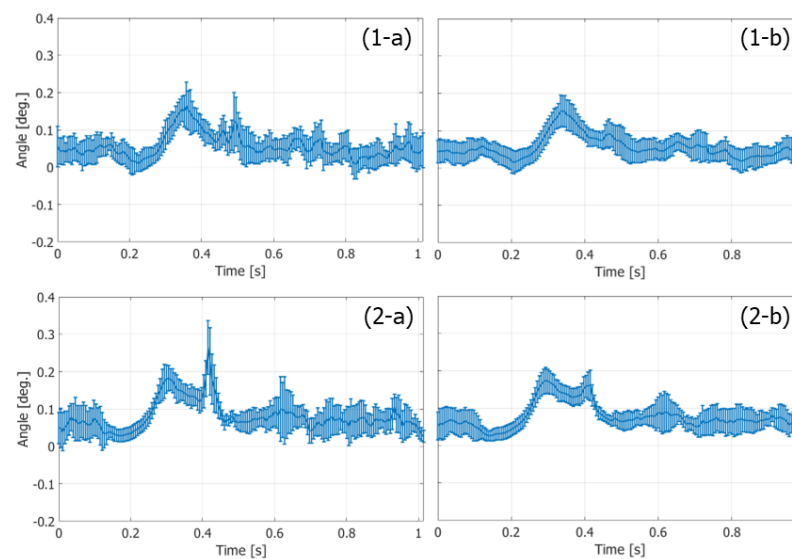


Figure 14. Temporal changes in means (plots) and standard deviations (vertical bars) of angles of velocity vectors at vertical center of ROI. (1-a,1-b) FB imaging. (2-a,2-b) PW imaging [48]. (1-a,2-a) Ensemble length of 23.04 ms. (1-b,2-b) Ensemble length of 46.04 ms.

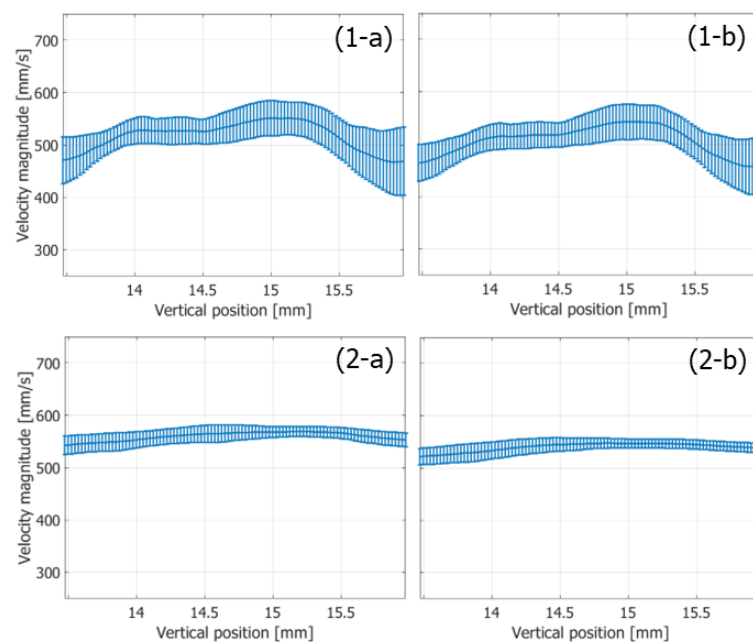


Figure 15. Means (plots) and standard deviations (vertical bars) of magnitudes of velocity vectors along the vertical axis at the time of the maximum mean velocity magnitude. (1-a,1-b) FB imaging. (2-a,2-b) PW imaging [48]. (1-a,2-a) Ensemble length of 23.04 ms. (1-b,2-b) Ensemble length of 46.04 ms.

Since the frame rate in the PW imaging was ten times higher than that in the FB imaging, overall standard deviations in the magnitudes of the estimated velocities were significantly lower in the PW imaging than in the FB imaging, owing to the significantly higher number of frames for averaging the complex correlation functions. However, similar maximum mean velocity magnitudes were obtained with both the FB and PW frameworks. On the other hand, there were not such large differences in the standard deviations in the angles of the velocity vectors estimated with the FB and PW frameworks, and the angle standard deviations were lower than 0.1 degrees.

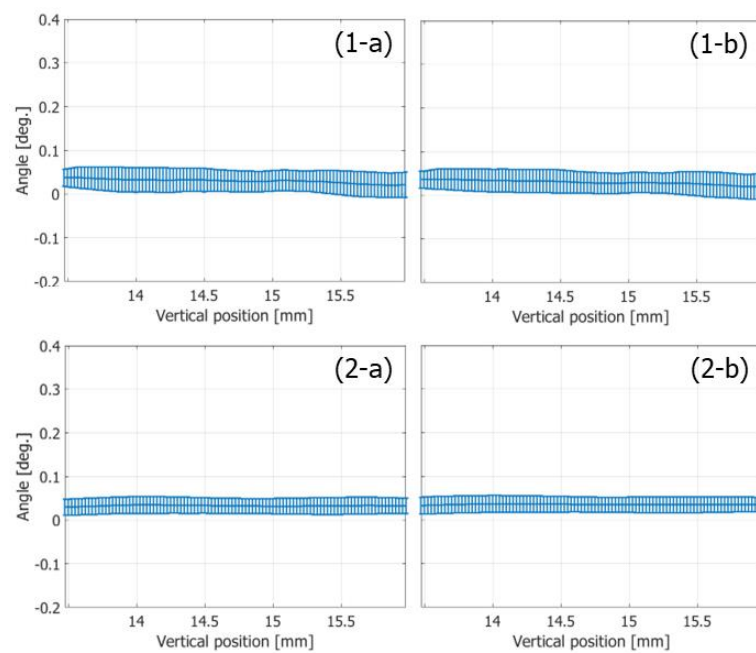


Figure 16. Means (plots) and standard deviations (vertical bars) of angles of velocity vectors along the vertical axis at the time of the maximum mean velocity magnitude. (1-a,1-b) FB imaging. (2-a,2-b) PW imaging [48]. (1-a,2-a) Ensemble length of 23.04 ms. (1-b,2-b) Ensemble length of 46.04 ms.

Finally, the proposed method was applied to a common carotid artery with a disturbed flow due to thickening of the arterial wall. The results are shown in Figure 17. Figure 17a–c show a normal B-mode image, a clutter-filtered B-mode image, and flow velocity vectors estimated in cardiac systolic phase overlaid on a blood speckle image, respectively. As can be seen in Figure 17c, a reasonable flow velocity distribution is also obtained for a disturbed flow by the proposed method.

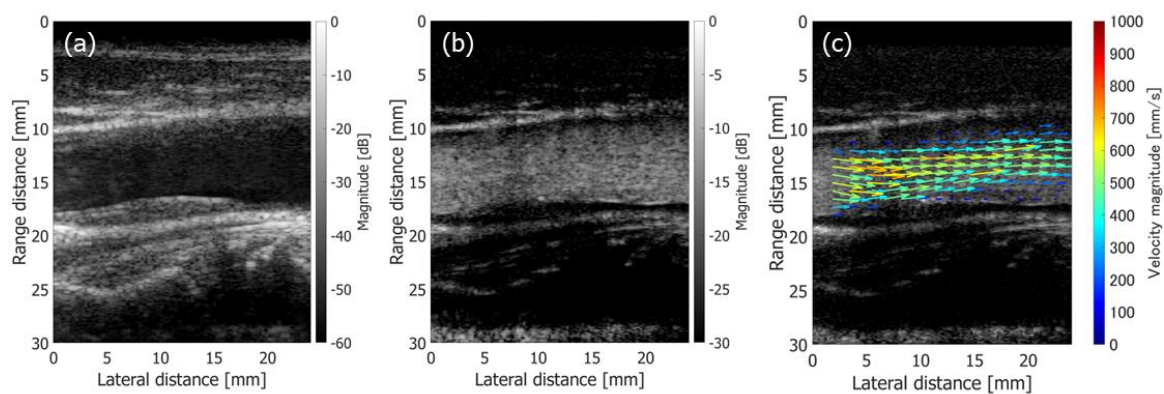


Figure 17. Results on in vivo measurement of a carotid artery with a disturbed flow due to wall thickening. (a) Normal B-mode image. (b) Clutter-filtered B-mode image. (c) Flow velocity vectors estimated in cardiac systolic phase are overlaid on blood speckle image.

4. Discussion

This study explored a strategy to implement the two-dimensional wavenumber analysis developed for PW imaging [48] in a multi-line Tx scheme with focused beams. In the focused beam sequence used in the present study, the Tx beam was not steered, and thus the Tx-Rx total steering angle becomes smaller as described in Section 2.3 than that in the case when both the Tx and Rx beams were steered [48]. Since a large Doppler angle increases the variance in estimated velocities [55], it was supposed that the variance was large using

our previous method in [41]. Our method for wavenumber analysis reduced the ambiguity in beam steering angles, and the variance in estimated velocities was reduced significantly.

The implementation of the two-dimensional wavenumber analysis was realized by parallel Rx beamforming. Parallel Rx beams are important to estimate the phase difference of the received signals in two neighboring Rx lines, owing to only the tilt of the wavefront because the phase difference would include a component induced by a target motion when the two Rx lines are obtained from different Tx's. Therefore, two parallel Rx lines were created in this study. Tilt angle ϕ of a wavefront in a beamformed signal induces a phase difference of $4\pi f_0 \delta x \sin \phi / c_0$. This phase difference is 1.34 radians at Rx line interval δx and wavefront tilt angle ϕ of 0.2 mm and 10 degrees, respectively, when the center frequency f_0 is 4.8 MHz. This phase difference should be less than π to avoid aliasing. Therefore, the lateral interval between the Rx lines should be narrowed when the proposed method is used with a higher center frequency or larger steering angle.

In this study, two Tx beams were also created in parallel to increase the frame rate. The Tx-Rx sequence requires (30 aperture positions) \times (2 Tx's per position) = 60 Tx's to acquire echo signals for one frame. Under such a condition, the frame rate becomes 174 frames per second (fps) when the PRI is 96 ms. This frame rate is far lower than that of 1736 fps in the vector Doppler method with PW imaging [48]. However, the frame rate in the proposed method is still significantly higher than that in conventional color flow imaging. To increase the number of parallel Tx beams is one of the strategies to increase the frame rate in the proposed method. However, as is reported in [40], the cross talks between the parallel Tx beams might be significant when the number of Tx beams is increased.

Although only two Tx beams were created in this study, the crosstalk between the two Tx beams affected the velocity estimation. In Figure 8, the errors in the estimated velocity vectors at flow tilt angle ϕ of 10 degrees are slightly larger than those at 0 and 5 degrees. To consider the reason for this phenomenon, B-mode images of the simulation phantoms at flow tilt angles ϕ of 0 and 10 degrees are shown in Figure 18a,b, respectively. The Rx beam steering angles were set at -20 degrees in both cases. It should be noted that the B-mode images are displayed with a large dynamic range of 80 dB. In Figure 18a, the crosstalk artifact is found beneath the simulation phantom. In Figure 18b, such an artifact is considered overlapping with the simulation phantom due to the tilt of the phantom and affected the velocity estimation.

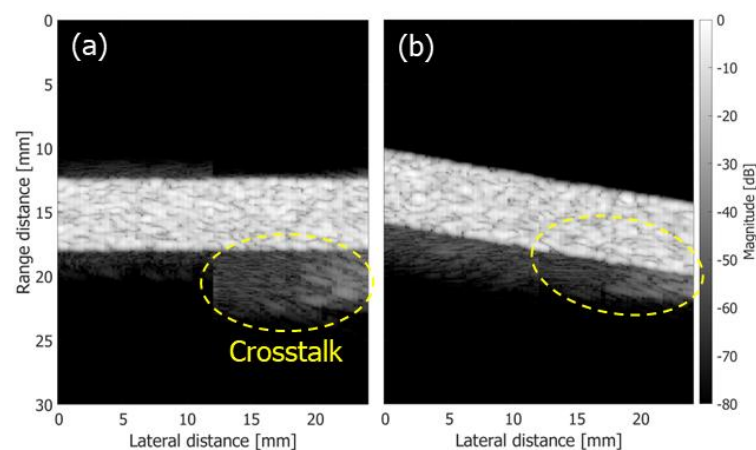


Figure 18. B-mode images obtained from beamformed signals with receiving steering angles of 20 degrees displayed at a dynamic range of 80 dB. (a) $\phi = 0$ degrees. (b) $\phi = 10$ degrees.

Even if the frame rate in the vector Doppler method with a focused beam strategy could be increased further, the high-frame-rate imaging with unfocused Tx beams such as a plane wave would still achieve a significantly higher frame rate. Such a high frame rate is considered beneficial for blood flow imaging. In Figure 12b, the contrast in the clutter-filtered B-mode image obtained with PW imaging is significantly higher in the

fast-flow phase than that with FB imaging. In SVD clutter filtering, the temporal intervals between the datasets were 5.76 and 0.576 μ s in the FB and PW frameworks, respectively. Due to the large temporal interval in the FB imaging, a significant part of signals might behave as echoes from slowly moving targets due to the aliasing phenomenon and removed by clutter filtering. At the diastolic notch (around 0.5 s), another significant decrease occurs in the contrast obtained with the FB framework because the difference between velocities of the blood flow and arterial wall becomes smaller due to an increase in the motion velocity of the arterial wall and a decrease in the blood flow velocity. On the other hand, although there were some fluctuations, consistent contrast values were obtained by PW imaging throughout a cardiac cycle. In addition, as shown in Figures 13 and 15, the PW framework achieved significant smaller standard deviations in velocity magnitudes than the FB framework. These facts prove the significant benefits of PW imaging in blood flow measurements.

The benefit of the proposed method with FB imaging is the high contrast between vessel lumen and surrounding tissue in normal B-mode imaging. Such a benefit might be further enhanced by implementing tissue harmonic imaging in the proposed method with FB imaging because tissue harmonic imaging is difficult in PW imaging due to the inherently lower sound pressure than in FB imaging. A strategy to implement the pulse inversion technique, which is an effective method for extracting harmonic components, should be explored to realize tissue harmonic imaging in the proposed method.

As described above, both FB and PW imaging have benefits and shortcomings. The implementation of the vector Doppler method in FB imaging presented in this paper adds a new choice for simultaneous observation of blood flow and surrounding tissue. On the other hand, PW imaging has predominant properties for blood flow imaging. Thus, a time division sequence including both FB emissions for tissue imaging and PW emissions for blood flow imaging is another possibility for optimal imaging of vascular dynamics. In such a time division sequence, the number of emissions available for clutter filtering should be limited, and clutter filtering in such a time division sequence might be one of the topics to be investigated. Development of an effective clutter filter with a small number of emissions would also be beneficial for the proposed FB framework to enable real-time imaging. Since the beamformed signals for approximately 1 s were used for clutter filtering with SVD, the proposed FB framework described in this paper cannot be performed in real time. An effective clutter filter, which works well with a smaller number of frames, would be required for real-time imaging.

Cardiac blood flow imaging is also important for the evaluation of heart function. The multi-line acquisition with FBs was used for myocardial motion imaging [40]. Clutter filtering with SVD is commonly used for vascular flow imaging [53] and is not common in cardiac flow imaging where more clutter motion is present. Although SVD was shown to be effective for clutter filtering in high-frame-rate cardiac flow imaging with diverging wave emissions [56], the feasibility in multi-line acquisition with a significantly lower frame rate has not been demonstrated. Further investigations are necessary to apply the proposed FB framework to cardiac flow imaging.

5. Conclusions

In this study, the two-dimensional wavenumber analysis was implemented in a multi-line Tx sequence with focused beams to improve the velocity estimates in the vector Doppler method. It was shown by the simulations that the proposed method could estimate the velocity vectors with RMSEs of approximately 10%, and the *in vivo* experimental results showed physiologically consistent velocity distributions in the two healthy subjects. The proposed method realized vector flow mapping at a frame rate of 174 fps, which is significantly higher than that in conventional color flow imaging. Such a method would be beneficial for detailed analyses of blood flow dynamics. The effectiveness of the proposed method in more complexly diseased arteries will be investigated in our future work.

Author Contributions: Conceptualization, H.H., M.O. and R.N.; methodology, H.H.; software, H.H.; validation, H.H.; formal analysis, H.H.; investigation, H.H., M.O., R.N. and K.S.; resources, H.H. and M.O.; data curation, H.H.; writing—original draft preparation, H.H.; writing—review and editing, H.H., M.O., R.N. and K.S.; visualization, H.H.; supervision, K.S.; project administration, H.H.; funding acquisition, H.H. All authors have read and agreed to the published version of the manuscript.

Funding: This work was supported by the JSPS KAKENHI number 18KK0110.

Institutional Review Board Statement: The study was conducted in accordance with the Declaration of Helsinki and approved by the Institutional Ethics Committees of University of Toyama (protocol code: R2015150, date of approval: 30 March 2016) and Nara Medical University (protocol code: 2465, date of approval: 14 November 2019).

Informed Consent Statement: Informed consent was obtained from all subjects involved in the study.

Data Availability Statement: Not applicable.

Acknowledgments: The authors thank Kerrie Gray at the University of Toyama for English proofreading.

Conflicts of Interest: The authors declare no conflict of interest.

References

1. Kasai, C.; Namekawa, K.; Koyano, A.; Omoto, R. Real-time two-dimensional blood flow imaging using an autocorrelation technique. *IEEE Trans. Sonics Ultrason.* **1985**, *32*, 458–464. [[CrossRef](#)]
2. Asami, R.; Tanaka, T.; Shimizu, M.; Seki, Y.; Nishiyama, T.; Sakashita, H.; Okada, T. Ultrasonic vascular vector flow mapping for 2-D flow estimation. *Ultrasound Med. Biol.* **2019**, *45*, 1663–1674. [[CrossRef](#)] [[PubMed](#)]
3. Trahey, G.E.; Allison, J.W.; von Ramm, O.T. Angle independent ultrasonic detection of blood flow. *IEEE Trans. Biomed. Eng.* **1987**, *34*, 965–967. [[CrossRef](#)] [[PubMed](#)]
4. Bohs, L.N.; Friemel, B.H.; Trahey, G.E. Experimental velocity profiles and volumetric flow via two-dimensional speckle tracking. *Ultrasound Med. Biol.* **1995**, *21*, 885–898. [[CrossRef](#)]
5. Takahashi, H.; Hasegawa, H.; Kanai, H. Echo speckle imaging of blood particles with high-frame-rate echocardiography. *Jpn. J. Appl. Phys.* **2014**, *53*, 07KF08. [[CrossRef](#)]
6. Fadnes, S.; Nyernes, S.A.; Torp, H.; Lovstakken, L. Shunt flow evaluation in congenital heart disease based on two-dimensional speckle tracking. *Ultrasound Med. Biol.* **2014**, *40*, 2379–2391. [[CrossRef](#)]
7. Takahashi, H.; Hasegawa, H.; Kanai, H. Echo motion imaging with adaptive clutter filter for assessment of cardiac blood flow. *Jpn. J. Appl. Phys.* **2015**, *54*, 07HF09. [[CrossRef](#)]
8. Nyernes, S.A.; Fadnes, S.; Wiggen, M.S.; Mertens, L.; Lovstakken, L. Blood speckle-tracking based on high-frame rate ultrasound imaging in pediatric cardiology. *J. Am. Soc. Echocardiogr.* **2020**, *33*, 493–503. [[CrossRef](#)]
9. Dunmire, B.; Beach, K.W.; Labs, K.H.; Plett, M.; Strandness, D.E., Jr. Cross-beam vector Doppler ultrasound for angle-independent velocity measurements. *Ultrasound Med. Biol.* **2000**, *26*, 1213–1235. [[CrossRef](#)]
10. Fahrback, K.K. Apparatus for Measuring the Speed of Flowing Media. U.S. Patent 3,766,517, 16 October 1973.
11. Peronneau, P.; Bournat, J.P.; Bugnon, A.; Barbet, A.; Xhaard, M. Theoretical and practical aspects of pulsed Doppler flowmetry real-time application to the measure of instantaneous velocity profiles in vitro and in vivo. In *Cardiovascular Applications of Ultra-Sound*; Reneman, R.S., Ed.; North Holland Publishing: Amsterdam, The Netherlands, 1974; pp. 66–84.
12. Peronneau, P.; Sandman, W.; Xhaard, M. Blood flow patterns in large arteries. In *Ultrasound in Medicine*; White, D.N., Brown, R.E., Eds.; Plenum Press: New York, NY, USA, 1977; pp. 1193–1208.
13. Fox, M.D. Multiple crossed-beam ultrasound Doppler velocimetry. *IEEE Trans. Son. Ultrason.* **1978**, *25*, 281–286. [[CrossRef](#)]
14. Steel, R.; Ramnarine, K.V.; Davidson, F.; Fish, P.J.; Hoskins, P.R. Angle-independent estimation of maximum velocity through stenoses using vector Doppler ultrasound. *Ultrasound Med. Biol.* **2003**, *29*, 575–584. [[CrossRef](#)]
15. Tortoli, P.; Dallai, A.; Boni, E.; Francalanci, L.; Ricci, S. An automatic angle tracking procedure for feasible vector Doppler blood velocity measurements. *Ultrasound Med. Biol.* **2010**, *36*, 488–496. [[CrossRef](#)]
16. Jensen, J.A.; Munk, P. A new method for estimation of velocity vectors. *IEEE Trans. Ultrason. Ferroelectr. Freq. Control* **1998**, *45*, 837–851. [[CrossRef](#)]
17. Tanter, M.; Bercoff, J.; Sandrin, L.; Fink, M. Ultrafast compound imaging for 2-D motion vector estimation: Application to transient elastography. *IEEE Trans. Ultrason. Ferroelectr. Freq. Control* **2002**, *49*, 1363–1374. [[CrossRef](#)] [[PubMed](#)]
18. Udesen, J.; Gran, F.; Hansen, K.; Jensen, J.A.; Thomsen, C.; Nielsen, M.B. High frame-rate blood vector velocity imaging using plane waves: Simulations and preliminary experiments. *IEEE Trans. Ultrason. Ferroelectr. Freq. Control* **2008**, *55*, 1729–1743. [[CrossRef](#)] [[PubMed](#)]
19. Hasegawa, H.; Kanai, H. Simultaneous imaging of artery-wall strain and blood flow by high frame rate acquisition of RF signals. *IEEE Trans. Ultrason. Ferroelectr. Freq. Control* **2008**, *55*, 2626–2639. [[CrossRef](#)] [[PubMed](#)]
20. Montaldo, G.; Tanter, M.; Bercoff, J.; Benech, N.; Fink, M. Coherent plane-wave compounding for very high frame rate ultrasonography and transient elastography. *IEEE Trans. Ultrason. Ferroelectr. Freq. Control* **2009**, *56*, 489–506. [[CrossRef](#)] [[PubMed](#)]

21. Bercoff, J.; Montaldo, G.; Loupas, T.; Savery, D.; Mézière, F.; Fink, M.; Tanter, M. Ultrafast compound Doppler imaging: Providing full blood flow characterization. *IEEE Trans. Ultrason. Ferroelectr. Freq. Control* **2011**, *58*, 134–147. [[CrossRef](#)] [[PubMed](#)]
22. Ricci, S.; Bassi, L.; Tortoli, P. Real-time vector velocity assessment through multigate Doppler and plane waves. *IEEE Trans. Ultrason. Ferroelectr. Freq. Control* **2014**, *61*, 314–324. [[CrossRef](#)]
23. Ricci, S.; Ramalli, A.; Bassi, L.; Boni, E.; Tortoli, P. Real-time blood velocity vector measurement over a 2-D region. *IEEE Trans. Ultrason. Ferroelectr. Freq. Control* **2018**, *65*, 201–209. [[CrossRef](#)]
24. Rossi, S.; Ramalli, A.; Tortoli, P. On the depth-dependent accuracy of plane-wave-based vector velocity measurements with linear arrays. *IEEE Trans. Ultrason. Ferroelectr. Freq. Control* **2021**, *68*, 2707–2715. [[CrossRef](#)] [[PubMed](#)]
25. Ekroll, I.K.; Swillens, A.; Segers, P.; Dahl, T.; Torp, H.; Lovstakken, L. Simultaneous quantification of flow and tissue velocities based on multi-angle plane wave imaging. *IEEE Trans. Ultrason. Ferroelectr. Freq. Control* **2013**, *60*, 727–738. [[CrossRef](#)] [[PubMed](#)]
26. Yiu, B.Y.S.; Lai, S.S.M.; Yu, A.C.H. Vector projectile imaging: Time-resolved dynamic visualization of complex flow patterns. *Ultrasound Med. Biol.* **2014**, *40*, 2295–2309. [[CrossRef](#)] [[PubMed](#)]
27. Yiu, B.Y.S.; Yu, A.C.H. Least-squares multi-angle Doppler estimators for plane wave vector flow imaging. *IEEE Trans. Ultrason. Ferroelectr. Freq. Control* **2016**, *63*, 1733–1744. [[CrossRef](#)] [[PubMed](#)]
28. Fadnes, S.; Ekroll, I.K.; Nyrnes, S.A.; Torp, H.; Lovstakken, L. Robust angle-independent blood velocity estimation based on dual-angle plane wave imaging. *IEEE Trans. Ultrason. Ferroelectr. Freq. Control* **2015**, *62*, 1757–1767. [[CrossRef](#)]
29. Saris, A.E.C.M.; Hansen, H.H.G.; Fekkes, S.; Nillesen, M.M.; Rutten, M.C.M.; de Korte, C.L. A comparison between compounding techniques using large beam-steered plane wave imaging for blood vector velocity imaging in a carotid artery model. *IEEE Trans. Ultrason. Ferroelectr. Freq. Control* **2016**, *63*, 1758–1771. [[CrossRef](#)]
30. Karageorgos, G.M.; Apostolakis, I.Z.; Nauleau, P.; Gatti, V.; Weber, R.; Kemper, P.; Konofagou, E.E. Pulse wave imaging coupled with vector flow mapping: A phantom, simulation, and in vivo Study. *IEEE Trans. Ultrason. Ferroelectr. Freq. Control* **2021**, *68*, 2516–2531. [[CrossRef](#)]
31. Lenge, M.; Ramalli, A.; Tortoli, P.; Cachard, C.; Liebgott, H. Plane wave transverse oscillation for high-frame-rate 2-D vector flow imaging. *IEEE Trans. Ultrason. Ferroelectr. Freq. Control* **2015**, *62*, 2126–2137. [[CrossRef](#)]
32. Perrot, V.; Ekroll, I.K.; Avdal, J.; Saxhaug, L.M.; Dalen, H.; Vray, D.; Løvstakken, L.; Liebgott, H. Translation of simultaneous vessel wall motion and vectorial blood flow imaging in healthy and diseased carotids to the clinic: A pilot study. *IEEE Trans. Ultrason. Ferroelectr. Freq. Control* **2021**, *68*, 558–569. [[CrossRef](#)]
33. Jensen, J.; Hoyos, C.A.V.; Stuart, M.B.; Ewertsen, C.; Nielsen, M.B.; Jensen, J.A. Fast plane wave 2-D vector flow imaging using transverse oscillation and directional beamforming. *IEEE Trans. Ultrason. Ferroelectr. Freq. Control* **2017**, *64*, 1050–1062. [[CrossRef](#)]
34. Lenge, M.; Ramalli, A.; Boni, E.; Liebgott, H.; Cachard, C.; Tortoli, P. High-frame-rate 2-D vector blood flow imaging in the frequency domain. *IEEE Trans. Ultrason. Ferroelectr. Freq. Control* **2014**, *61*, 1504–1514. [[CrossRef](#)] [[PubMed](#)]
35. Kaburaki, K.; Mozumi, M.; Hasegawa, H. Estimation of two-dimensional motion velocity using ultrasonic signals beamformed in Cartesian coordinate for measurement of cardiac dynamics. *Jpn. J. Appl. Phys.* **2018**, *57*, 07LF03. [[CrossRef](#)]
36. Tong, L.; Gao, H.; Choi, H.F.; D’hooge, J. Comparison of conventional parallel beamforming with plane wave and diverging wave imaging for cardiac applications: A simulation study. *IEEE Trans. Ultrason. Ferroelectr. Freq. Control* **2012**, *59*, 1654–1663. [[CrossRef](#)] [[PubMed](#)]
37. Tong, L.; Gao, H.; D’hooge, J. Multi-transmit beam forming for fast cardiac imaging—a simulation study. *IEEE Trans. Ultrason. Ferroelectr. Freq. Control* **2013**, *60*, 1719–1731. [[CrossRef](#)] [[PubMed](#)]
38. Tong, L.; Ramalli, A.; Jasaityte, R.; Tortoli, P.; D’hooge, J. Multi-transmit beam forming for fast cardiac imaging—Experimental validation and in vivo application. *IEEE Trans. Med. Imaging* **2014**, *33*, 1205–1219. [[CrossRef](#)]
39. Tong, L.; Ramalli, A.; Tortoli, P.; Fradella, G.; Cacioli, S.; Luo, J.; D’hooge, J. Wide-angle tissue Doppler imaging at high frame rate using multi-line transmit beamforming: An experimental validation in vivo. *IEEE Trans. Med. Imaging* **2015**, *35*, 521–528. [[CrossRef](#)]
40. Ramalli, A.; Dallai, A.; Guidi, F.; Bassi, L.; Boni, E.; Tong, L.; Fradella, G.; D’hooge, J.; Tortoli, P. Real-time high-frame-rate cardiac B-mode and tissue Doppler imaging based on multiline transmission and multiline acquisition. *IEEE Trans. Ultrason. Ferroelectr. Freq. Control* **2018**, *65*, 2030–2041. [[CrossRef](#)]
41. Hasegawa, H.; Mozumi, M.; Omura, M.; Nagaoka, R.; Saito, K. Preliminary study on estimation of flow velocity vectors using focused transmit beams. *Jpn. J. Appl. Phys.* **2022**, *61*, SG1026. [[CrossRef](#)]
42. Loupas, T.; Powers, J.T.; Gill, R.W. An axial velocity estimator for ultrasound blood flow imaging, based on a full evaluation of the Doppler equation by means of a two-dimensional autocorrelation approach. *IEEE Trans. Ultrason. Ferroelectr. Freq. Control* **1995**, *42*, 672–688. [[CrossRef](#)]
43. Rabben, S.I.; Baerum, S.; Sorhus, V.; Torp, H. Ultrasound-based vessel wall tracking: An auto-correlation technique with RF center frequency estimation. *Ultrasound Med. Biol.* **2002**, *28*, 507–517. [[CrossRef](#)]
44. Hasegawa, H.; Kanai, H. Modification of the phased-tracking method for reduction of artifacts in estimated artery wall deformation. *IEEE Trans. Ultrason. Ferroelectr. Freq. Control* **2006**, *53*, 2050–2064. [[CrossRef](#)] [[PubMed](#)]
45. Hasegawa, H.; Kanai, H.; Koiwa, Y. Modified phased tracking method for measurement of change in thickness of arterial wall. *Jpn. J. Appl. Phys.* **2002**, *41*, 3563–3571. [[CrossRef](#)]
46. Hasegawa, H.; Kanai, H. Reduction of influence of variation in center frequencies of RF echoes on estimation of artery-wall strain. *IEEE Trans. Ultrason. Ferroelectr. Freq. Control* **2008**, *55*, 1921–1934. [[CrossRef](#)] [[PubMed](#)]

47. Hasegawa, H.; Nagaoka, R.; Omura, M.; Mozumi, M.; Saito, K. Measurement of flow velocity vectors in carotid artery by plane wave imaging with repeated transmit sequence. *J. Med. Ultrason.* **2021**, *48*, 417–427. [[CrossRef](#)] [[PubMed](#)]
48. Hasegawa, H.; Omura, M.; Nagaoka, R. On the investigation of autocorrelation-based vector Doppler method with plane wave imaging. *IEEE Trans. Ultrason. Ferroelectr. Freq. Control* **2022**, *69*, 1301–1311. [[CrossRef](#)]
49. Jensen, J.A. A model for the propagation and scattering of ultrasound in tissue. *J. Acoust. Soc. Am.* **1991**, *89*, 182–190. [[CrossRef](#)]
50. Jensen, J.A.; Svendsen, N.B. Calculation of pressure fields from arbitrarily shaped, apodized, and excited ultrasound transducers. *IEEE Trans. Ultrason. Ferroelectr. Freq. Control* **1992**, *39*, 262–267. [[CrossRef](#)]
51. Podkowa, A.S.; Oelze, M.L.; Ketterling, J.A. High-frame-rate Doppler ultrasound using a repeated transmit sequence. *Appl. Sci.* **2018**, *8*, 227. [[CrossRef](#)]
52. Mahafza, B.R. *Introduction to Radar Analysis*; CRC Press: Boca Raton, FL, USA, 1998.
53. Demené, C.; Deffieux, T.; Pernot, M.; Osmanski, B.F.; Biran, V.; Gennisson, J.L.; Sieu, L.A.; Bergel, A.; Franqui, S.; Correas, J.M.; et al. Spatiotemporal clutter filtering of ultrafast ultrasound data highly increases Doppler and ultrasound sensitivity. *IEEE Trans. Med. Imaging* **2015**, *34*, 2271–2285. [[CrossRef](#)]
54. Zócalo, Y.; Bia, D. Sex- and age-related physiological profiles for brachial, vertebral, carotid, and femoral arteries blood flow velocity parameters during growth and aging (4–76 years): Comparison with clinical cut-off levels. *Front. Physiol.* **2021**, *12*, 729309. [[CrossRef](#)]
55. Park, M.Y.; Jung, S.E.; Byun, J.Y.; Kim, J.H.; Joo, G.E. Effect of beam-flow angle on velocity measurements in modern Doppler ultrasound systems. *Am. J. Roentgenol.* **2012**, *198*, 1139–1143. [[CrossRef](#)] [[PubMed](#)]
56. Mozumi, M.; Nagaoka, R.; Hasegawa, H. Utilization of singular value decomposition in high-frame-rate cardiac blood flow imaging. *Jpn. J. Appl. Phys.* **2019**, *58*, SGGE02. [[CrossRef](#)]